Simulating the Formation of Fine-Scale Structure in Saturn's Rings

Heikki Salo*)

Division of Astronomy, Department of Physics, PL 3000, FI-90014 University of Oulu, Finland

Planetary ring dynamics is reviewed, based on the results of local 3-dimensional simulations, which utilize a co-moving calculation cell with periodic boundary conditions. Various factors affecting the local balance between collisional dissipation and viscous gain of energy from the systematic velocity field are considered, including gravitational encounters and collective gravitational forces besides physical impacts. Simulation examples of the effects of different forms of the coefficient of restitution are given. Viscous stability properties are also discussed: examples of both instabilities and overstabilities are given and briefly discussed in the context of observed structures in Saturn's rings.

§1. Introduction

Saturn's rings consist of cm to meter-sized icy particles revolving on nearly circular, almost co-planar orbits. The ring evolution is governed by the orbital motion, the frequent impacts between ring particles, their mutual self-gravity, and the perturbations exerted by both external satellites and by embedded moonlets. In the dense main rings (the A and B rings) particles collide even 10–100 times per orbital revolution. Although the orbital velocities are ~ 20 km/s, the random velocities related to orbital eccentricities and inclinations are small, indicating impact velocities below ~ 0.5 cm/s (corresponds to ring vertical thickness ~ 10 meters). Such gentle impacts do not lead to fragmentation, but still dissipate a significant fraction of random kinetic energy in each collision. This loss is balanced by the viscous gain of energy from the differential rotation around the planet (orbital speeds increase inward), establishing a local steady-state in a time scale of few tens of impacts/particle.[16),21),56)] Details of the resulting balance (velocity dispersion, geometric thickness, viscosity) are determined by the frequency and elasticity of impacts, and the internal density and size distribution of particles.[43)] Depending on the implied viscosity-density relation, the ring can be either stable or unstable against the growth of local perturbations. For example, dense rings composed of quite inelastic particles can become viscously overstable, which is likely to relate to the strictly axisymmetric small-scale oscillations observed in several locations of Saturn's A and B rings.[9),58)]

The importance of ring particles' mutual gravity for shaping the local structure of Saturn's rings has been strikingly demonstrated by the Cassini stellar[8),9),19)] and radio occultation measurements,[58)] which confirm the presence of unresolved trailing structures (self-gravity wakes[41)]) throughout the A and B rings. These structures arise as a superposition of tiny perturbations excited around each individual ring particle, amplified by the interplay of shear and gravity (swing-amplification mechanism[61)]). Such structures were envisioned by Alar Toomre already decades

*) E-mail: heikki.salo@oulu.fi

ago,[23] though in a very different context (and scale — kpcs rather than meters), as a suggestion of how to create and maintain spiral structure in galactic disks. The crucial ingredient in planetary rings is the mutual dissipative impacts between particles, which keep the ring dynamically cool and thus reactive to gravitational disturbances. Self-gravity wakes are just one example: similarly the excitation of spiral density waves at the satellite resonance locations has the clearest manifestation in Saturn's rings;[7] Saturn's rings also provide the most extreme examples of disk warping,[20] and the effect of embedded mass concentrations on the surrounding particles ('propellers').[12]

This paper reviews numerical simulations of self-gravitating, mutually colliding particles, using a local method (Appendix A) where the evolution of a small comoving ring patch is followed. Besides illustrating the basic mechanisms leading to local energy balance (§2), simulation examples of self-gravity wakes (§3) and nonlinear structures resulting from viscous overstability and instability are presented (§4). For detailed theoretical background (covering also perturbations by external and embedded satellites, see Ref. 51); also the articles by J. Burns, K. Ohtsuki, and J. Schmidt in these proceedings).

§2. Local energy balance

The fundamental quantity describing both the dynamics and observed structures of Saturn's rings is the geometric optical depth τ, defined as the fractional surface area covered by particles. One peculiarity of ring dynamics is the independence of impact frequency ω_c from the velocity dispersion c,

$$\omega_c \sim 3\tau\Omega \sim 20\tau \text{ impacts/orbit}, \tag{2·1}$$

where Ω is the angular orbital frequency. This results from the partitioning of vertical and horizontal random motions in impacts, which, combined with the fact that the particles are revolving around the planet, implies that any increase in velocity dispersion is compensated by the corresponding thickening of the ring, which leads to reduced space density.*)

Locally, the ring establishes a steady-state between the viscous gain of energy from the differential rotation associated with the orbital motion and the energy dissipated in inelastic impacts. The time-scale to achieve this is a few tens of impacts per particle, or just a couple of days for $\tau \gtrsim 1$. On much longer time-scales, the intrinsic ring evolution is determined by the radial flow of angular momentum: the stability properties of this flow depend sensitively on the elastic properties of particles via the implied local energy balance. The crucial factor is the functional dependence of steady-state viscosity ν on density, parameterized as $\nu \propto \tau^\beta$.

*) The basic formula is $\omega_c \propto n_s c \sigma_c$, where n_s is the space number density, c is the 1-dimensional velocity dispersion and σ_c the collisional cross-section: $\sigma_c = 4\pi R^2$ assuming identical particles with radius R. The space density $n_s \approx n/H$, where $n = \tau/(\pi R^2)$ is the surface number density and H the vertical thickness. Due to collisional coupling of horizontal and vertical motions, $c_z \sim c$, while due to orbital motion $H \propto c_z/\Omega$. The explicit n_s and c dependence thus cancels out, leading to formula (2·1). Note that self-gravity can lead to significantly enhanced ω_c (§3).

The main source of dissipation is the inelasticity of impacts, measured by the normal coefficient of restitution $\varepsilon_{\rm n}$,

$$\dot{E}_{diss} = k_1\ \omega_c\ c^2(1-{\varepsilon_{\rm n}}^2), \tag{2·2}$$

(k_1, like k_2 and k_3 below is a numerical factor of order unity; in the case of velocity-dependent elasticity $\varepsilon_{\rm n}$ is defined as an effective mean value averaged over impacts.) The gain is proportional to kinematic viscosity and the square of the shear rate,

$$\dot{E}_{gain} = \left(r\frac{\partial\Omega}{\partial r}\right)^2 \nu \equiv s^2\nu. \tag{2·3}$$

For particles orbiting a central planet $\Omega(r) \propto r^{-3/2}$ so that $s = -\frac{3}{2}\Omega$. In the case of non-gravitating particles, the viscosity is usually divided to two contributions, the local viscosity ν_l associated with the transport of angular momentum via the particle's radial excursions, and the non-local viscosity ν_{nl} resulting from the momentum transferred from one particle to another during a collision (the gravitational viscosity ν_{grav} arising due to torques exerted by non-axisymmetric collective structures formed via self-gravity is discussed in §3). The basic expression for local viscosity is $\nu_l = \omega_c\lambda^2$, where λ is the radial mean free path. In the high impact frequency regime the impacts limit the mean free path to $\lambda \sim c/\omega_c$ while for low ω_c an upper bound is set by the amplitude of epicyclic excursions, $\lambda \sim c/\Omega$. Combining these estimates[16] $\nu_l = k_2\,\omega_c c^2/({\omega_c}^2 + \Omega^2)$. For the nonlocal momentum transfer, $\nu_{nl} = k_3\ \omega_c R^2$, where R is the particle radius. The energy balance $\dot{E}_{diss} = \dot{E}_{gain}$ thus implies

$$k_1\,\omega_c\,c^2(1-{\varepsilon_{\rm n}}^2) = \frac{9}{4}\omega_c c^2\left[\frac{k_2}{1+(\omega_c/\Omega)^2} + k_3\left(\frac{R\Omega}{c}\right)^2\right]. \tag{2·4}$$

Although Eq. (2·4) is based on simple heuristic arguments,[56] it describes qualitatively quite well the simulated behavior for a given elasticity of particles. In particular, if the system is very hot, $c/(R\Omega) \gg 1$, the nonlocal gain term can be ignored, and the energy balance requires that the effective value of ε_n attains a critical value $\varepsilon_{\rm cr}$, which (approximating $\omega_c \sim \Omega\tau$) depends on the optical depth via the well-known Goldreich-Tremaine formula[16]

$$(1-{\varepsilon_{\rm cr}}^2)(1+\tau^2) = \frac{9k_2}{4k_1} \approx 0.61. \tag{2·5}$$

In the case of constant $\varepsilon_{\rm n} > \varepsilon_{\rm cr}$, no energy balance can be achieved, as the dissipation is then too weak to balance the local viscous gain: the system disperses via continuously growing random velocities. The critical $\varepsilon_{\rm cr}$ increases with τ (Fig. 1), since the reduced mean free path between impacts limits the local gain: $\varepsilon_{\rm cr}(\tau \to 0) \approx 0.65$, while $\varepsilon_{\rm cr}(\tau = 1) \approx 0.8$*) On the other hand if the constant $\varepsilon_{\rm n} < \varepsilon_{\rm cr}$, the dissipation exceeds the local viscous gain, leading to reduced eccentricities and inclinations. The eventual steady-state is then determined by the nonlocal viscous gain (second term

*) Allowing for tangential friction in impacts would shift $\varepsilon_{\rm cr}$ even closer to unity, as the frictional loss would add to the dissipation due to inelasticity.[32),40)]

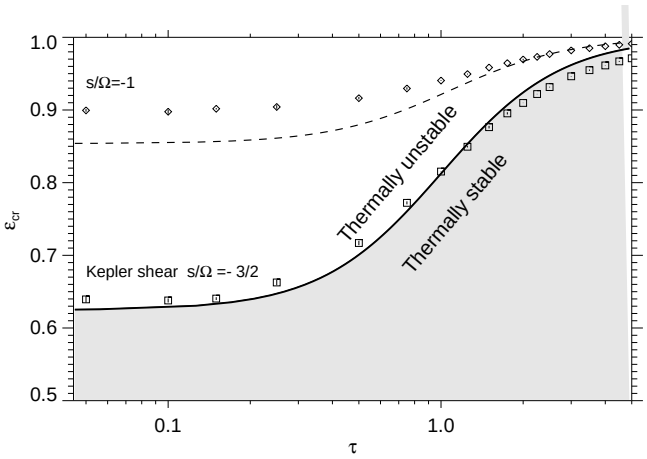

Fig. 1. The solid line indicates the Goldreich-Tremaine $\varepsilon_{\rm cr}(\tau)$ relation. Systems with constant $\varepsilon_{\rm n} < \varepsilon_{\rm cr}(\tau)$ (shaded region) flatten toward a stable near-monolayer state, while those with $\varepsilon_{\rm n} > \varepsilon_{\rm cr}(\tau)$ disperse via growing random velocities. Also shown is an approximative critical curve for a flat velocity field with $s/\Omega = -1$ (dashed line; obtained by replacing 9/4 with 1 in 2·5): the energy gain from systematic velocity is reduced, allowing energy balance take place for $\varepsilon_{\rm n}$ closer to unity. Symbols indicate effective values of $\varepsilon_{\rm n}$ attained in dynamically hot simulations with $c/(\Omega R) \gg 1$, thus approximating the conditions leading to 2·5).

on rhs of (2·4)), and corresponds to a flattened system where the geometric thickness is of the order of few particle diameters, $H \sim R$ (in terms of random velocities $c \sim R\Omega$).

In the realistic case $\varepsilon_{\rm n}$ depends on the impact velocity v_n. The value of steady-state velocity dispersion depends then on the form of $\varepsilon_{\rm n}(v_n)$, as the system adjusts its effective $\varepsilon_{\rm n}$ according to Eq. (2·4). The steady-state can range from a thick multilayer ($H \gg R$) to a near monolayer ring ($H \sim R$). The laboratory measurements in Refs. 5) and 18) indicated that $\varepsilon_{\rm n}$ drops to values significantly below unity already for impact velocities of the order of 1 cm/sec. However, the exact form of $\varepsilon_{\rm n}(v_n)$ relation is sensitive to the surface properties of ice — hardly known for the physical conditions of the rings — as well as on the particle size, via the curvature of the impact point.

Figure 2a) depicts two elasticity model curves, illustrating the wide range of uncertainty concerning particles' elastic properties. The large uncertainty reflects directly to the simulated steady-state. A system of fairly elastic 'smooth' particles is dynamically hot at low τ (Fig. 2b)) but exhibits a large (by a factor ~ 5) reduction of velocity dispersion as $\tau \gtrsim 1$, basically because of the above-mentioned suppression of the local viscous gain as the mean free path shortens: the behavior corresponds closely to the mass-point simulations depicted in Fig. 1. On the other hand, the dynamically cool 'frosty' particle model has a nearly constant velocity dispersion with τ, behaving like a constant $\varepsilon_{\rm n} < \varepsilon_{\rm cr}$.

Most importantly, the two elastic models lead to a qualitatively different ν vs τ relation and thus have different viscous stability properties (Figs. 2c) and d)). For the smooth particle model the drop in ν_l is so strong that it establishes $\beta < -1$ for an

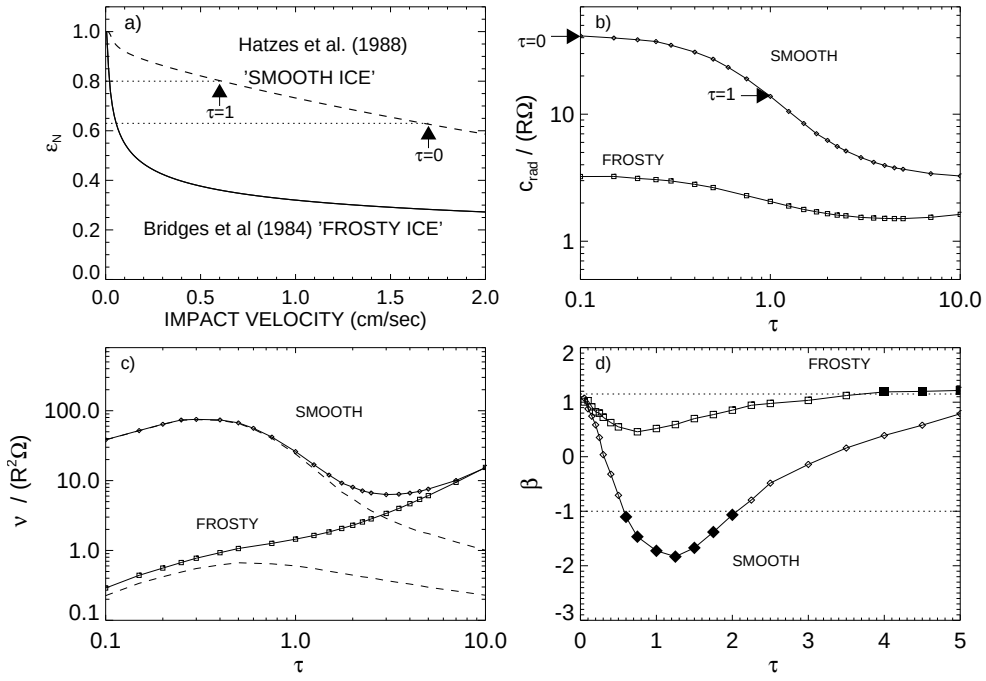

Fig. 2. a) Two elasticity models based on laboratory experiments, illustrating the range of uncertainty concerning particles' physical properties. The solid curve refers to measurements of frost-covered ice,[5] $\varepsilon_{\rm n}(v_n) = 0.32(v_n)^{-0.234} < 1$, and dashed curve to particles with compacted-frost surfaces (20 cm particles at temperature of 123 K),[18] $\varepsilon_{\rm n}(v_n) = 0.90e^{-0.22v_n} + 0.01{v_n}^{-0.6}$ (v_n expressed in cm/sec). b) Simulated radial velocity dispersion c_{rad} in units of $R\Omega$. c) Kinematic viscosity in units of $R^2\Omega$: dashed line shows separately the local contribution. d) The slope of $\nu \propto \tau^\beta$ relation: values of $\beta < -1$ (filled diamonds) indicate viscous instability, while $\beta \gtrsim 1$ (filled boxes) corresponds to viscous overstability.

interval $0.6 \lesssim \tau \lesssim 2$; eventually ν_{nl} takes over and β increases again. Such a system is prone for *viscous instability*. On the other hand, the frosty particle model implies a monotonically increasing ν due to the nonlocal part, with β even exceeding unity for $\tau \gtrsim 4$, indicating that the system becomes susceptible to *viscous overstability*. Note that the simulations used in Fig. 2 for tabulating the steady-state properties are *all* stable: the system size ($\lesssim 50$ particle radii) has deliberately been kept smaller than the minimum unstable wavelengths, thus suppressing any instabilities which would rise in larger systems.*) In §4 direct examples of both viscous instabilities and overstabilities are shown, using larger-scale simulations. However, before that §3 describes the effects of self-gravity, which has a significant effect on the viscosity.

*) To reduce the statistical noise following from a small system size and a small particle number ($N = 500 - 4000$), the simulation values were collected as time averages over at least 100 orbital periods, once the steady-state was established within the first few or few tens of orbital periods.

§3. Ring self-gravity

The rings of Saturn reside inside the planet's Roche-zone, so that direct gravitational accumulation of ring particles to form a satellite is prevented by the disruptive effect of planet's tidal force. Also, the total mass of the rings is only $\sim 10^{-8} M_{plan}$. Nevertheless, due to the low velocity dispersion maintained by the frequent dissipative impacts, the mutual gravity between particles can have a strong effect on the ring structure and evolution, depending on the local ring density and the distance from the planet.

At low τ the main effect is the gravitational scattering in close binary encounters. Since these correspond to totally elastic impacts, they conserve the kinetic energy of the encountering pair, while the deflection of the orbits transports energy from systematic motion to random motions. This extra heating increases c until it becomes comparable to particles' escape velocity.[11),21)] When the surface density Σ increases, the collective effects become important. For example, in the dense B and A rings, the vertical self-gravity exceeds the vertical component of the central force. This means significantly enhanced impact frequency, and reduced vertical thickness (Fig. 3). As a consequence, the viscosity (due to enhanced ν_{nl}) rises much steeper with τ than in the absence of vertical gravity.

However, whenever the vertical field becomes important, the system is also near the threshold of collective gravitational instability. Reference 60) showed that a self-gravitating differentially rotating particle disk is locally unstable against the growth of axisymmetric disturbances if its radial velocity dispersion falls below the critical value $c_{\rm cr} = 3.36 G\Sigma/\Omega_r$, where G is the gravitational constant and Ω_r the epicyclic frequency, nearly equal to Ω in planetary orbital motion. The closeness to the stability boundary is measured by the Toomre parameter

$$Q = c_{rad}/c_{\rm cr}. \tag{3·1}$$

While $Q \geq 1$ guarantees *axisymmetric* stability, already for $Q \lesssim 2-3$ the system is susceptible to the growth of local *non-axisymmetric* disturbances.[23)] This near-instability manifests as the emergence of trailing filamentary density enhancements, *gravity wakes*. In Keplerian velocity field they form $\sim 20^\circ$ angle with the tangential direction, while the radial separation is comparable to Toomre's critical wavelength

$$\lambda_{\rm cr} = 4\pi^2 G\Sigma/{\Omega_r}^2. \tag{3·2}$$

Thus with the inclusion of full self-gravity (Fig. 3c)), the picture is completely different from that when only the vertical component is taken into account. In particular, the viscosity is strongly enhanced.

Figure 4 displays wake structure in simulations where the calculation region is large enough to accommodate several wakes.*) It also illustrates the role of wakes/impacts in establishing a 'thermostat', keeping the system near the state $Q \sim 2$. In the case of stellar systems, originally studied by Toomre, the gravitational

*) As a rule of thumb, the simulation system should cover $4\lambda_{\rm cr} \times 4\lambda_{\rm cr}$, or preferentially more, to assure that the strength and orientation are not affected by the periodic boundaries[42),45)]

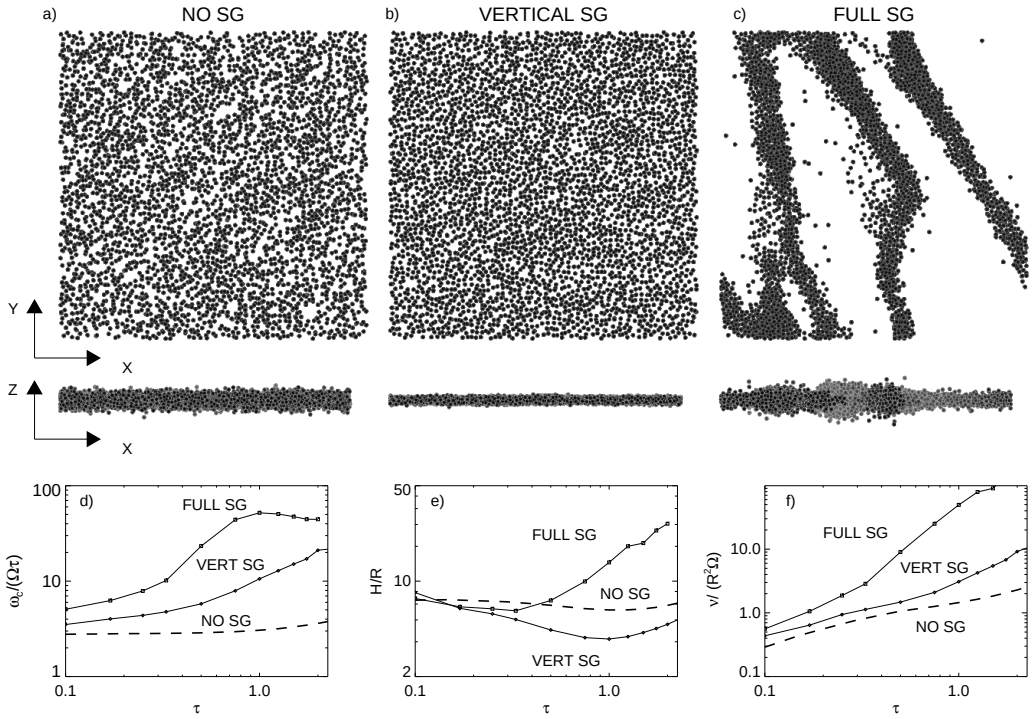

Fig. 3. Snapshots from $2\lambda_{\rm cr} \times 2\lambda_{\rm cr}$ simulations with $\tau = 0.75$, using the frosty particle elasticity model. In a) self-gravity is ignored, in b) only the vertical component and in c) all components of self-gravity are included. Frames d)–f) compare the impact frequency (normalized by $\Omega\tau$), the vertical thickness, and the kinematic viscosity as a function of optical depth. In the self-gravitating cases, solid ice density $\rho = 900$ kgm^{-3} is assumed. At the simulated Saturnocentric distance 100 000 km this corresponds to $r_h = 0.82$ according to Eq. (3·4).

scattering accompanying these disturbances heats the system so that the wakes are eventually suppressed — in the case of particulate rings, the collisional dissipation leads to a statistical steady-state, where new structures continuously emerge and dissolve in timescale comparable to orbital period. As stressed by Toomre,[62] the gravity wakes do not represent any instability in the sense that there would be strict threshold for the onset of wake structure; rather they manifest the reactivity of the system when Q is sufficiently small. In particular, any small leading perturbation, while evolving into a trailing one due to shear, is significantly amplified by the interplay of gravity and differential rotation ('swing amplification'[61]) The wake structure can be interpreted as a superposition of numerous individual wakes, excited by each particle when other particles flow past it. This picture is confirmed by the autocorrelation analysis of wakes.[42),45),62)]

In the non-gravitating case the optical depth τ and the particle elasticity $\varepsilon_{\rm n}$ determine the ring structure (in addition to particle size distribution). With the inclusion of self-gravity, one additional parameter is sufficient to characterize the importance of both the pairwise and collective gravitational effects. This is the r_h parameter, the ratio of the mutual Hill-radius for a pair of particles to the sum of

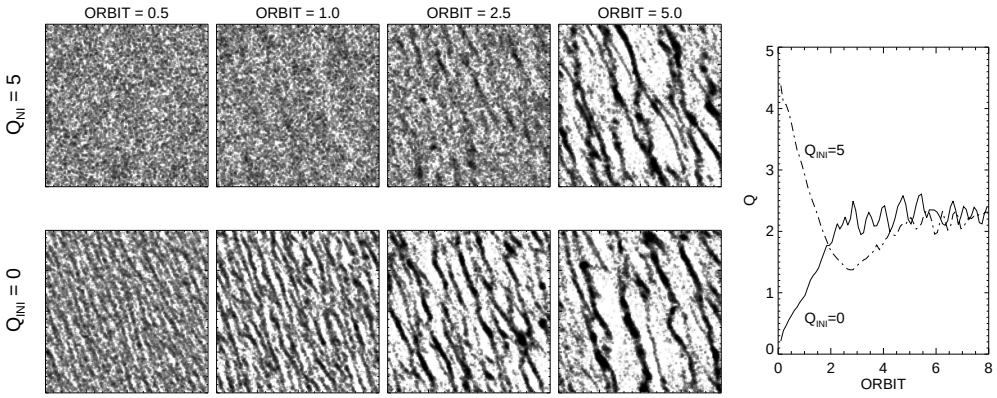

Fig. 4. Initial evolution in $8\lambda_{\rm cr} \times 8\lambda_{\rm cr}$ simulations starting with a hot ($Q = 5$) and cold ($Q = 0$) uniform initial state. The parameters are $\tau = 0.5$, $r_h = 0.82$, and $\varepsilon_{\rm n} = 0.5$.

their physical radii,

$$r_h(\mu) = \frac{R_{Hill}}{R_1 + R_2} = \left(\frac{\rho}{3\rho_{plan}}\right)^{1/3} \left(\frac{r}{r_{plan}}\right) \frac{(1+\mu)^{1/3}}{1+\mu^{1/3}}, \qquad (3{\cdot}3)$$

where ρ is the internal density of the ring particles, and $\mu = M_1/M_2 = (R_1/R_2)^3$ is their mass ratio. Here $R_{Hill} = ((M_1 + M_2)/3M_{plan})^{1/3} r$ is the radius of the Hill-sphere, where mutual gravity dominates over the tidal pull from the planet at the distance r. When r_h decreases, the particle pair, due to their physical size, extends more and more out from their Hill-sphere: $r_h = 0$ corresponds to the nongravitating case, while in the case $r_h = 1$ the attraction between two synchronously rotating, radially aligned ring particles in contact equals the disruptive tidal force. For $\mu = 1$, inserting the typical parameters for Saturn's rings yields

$$r_h(\mu = 1) = 0.82 \left(\frac{M_{plan}}{5.69 \cdot 10^{26}\ \mathrm{kg}}\right)^{-1/3} \left(\frac{\rho}{900\ \mathrm{kgm}^{-3}}\right)^{1/3} \left(\frac{r}{100\ 000\ \mathrm{km}}\right). \qquad (3{\cdot}4)$$

For a test particle attached to a large particle, the r_h is a factor $2^{2/3} \approx 1.59$ larger; in the following we denote $r_h(\mu = 1)$ simply by r_h. Assuming solid ice density ($\rho = 900\ \mathrm{kgm}^{-3}$), the main rings of Saturn extend $r_h = 0.6 - 1.1$: with the formula (3·4), the results for a given r_h can be scaled to any other $\rho^{1/3} r$ combination.

Figure 5 depicts a simulation survey of wake structures for $\varepsilon_{\rm n} = 0.5$. The strength of wakes increases when the optical depth τ, or the distance (measured with r_h) increases. The wakes also get clumpier and eventually degrade into semi-permanent gravitational aggregates for $r_h \gtrsim 1.2$. Same takes place at low τ via pairwise accumulation. The exact boundary depends on the elasticity of particles and also the particle size distribution.[24),42)] The fact that $r_h > 1$ is required for stable aggregates to form is because not only shear, but also particle impacts and velocity dispersion acts to destroy any forming condensations.

The insert in Fig. 5 sketches the parameter regimes where different factors (impacts, encounters, wakes) dominate the dynamics, based on the velocity dispersion

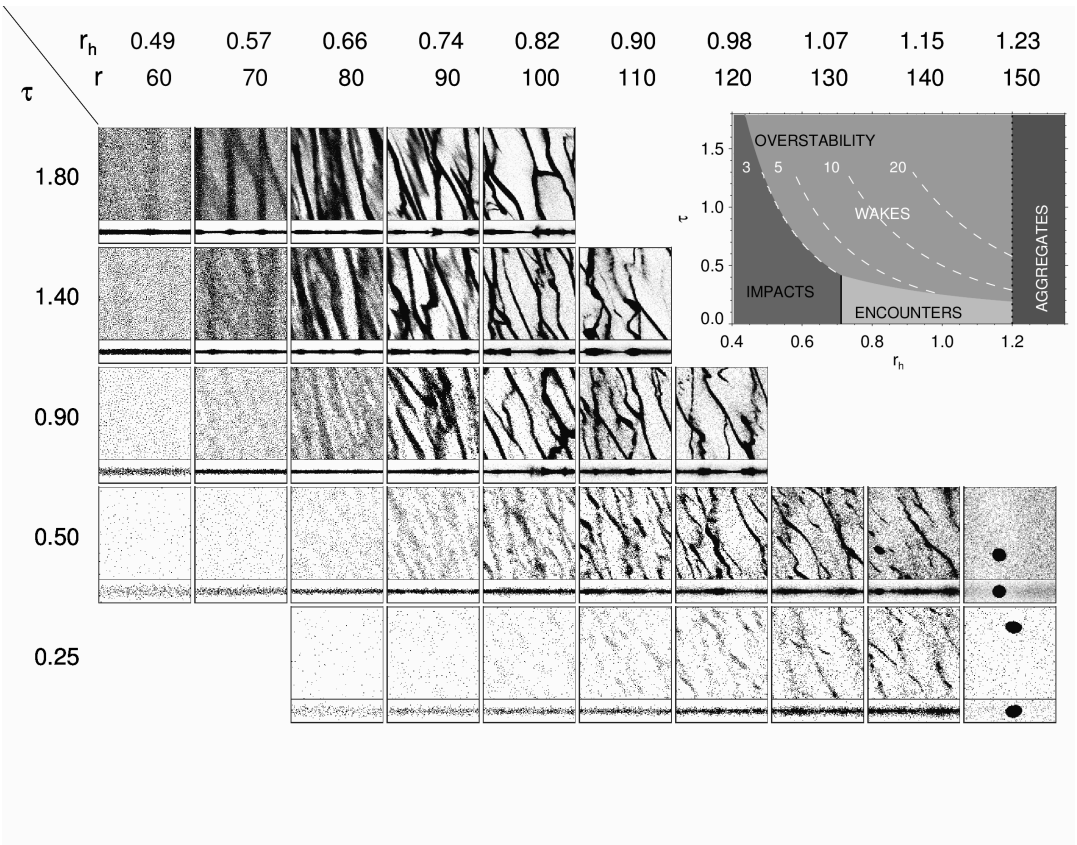

Fig. 5. Survey of self-gravity wakes as a function of r_h and τ, for constant $\varepsilon_{\rm n} = 0.5$. The labels r indicate the Saturnocentric distance (in units of 1000 km) for particles with solid ice internal density: for other densities the distances scale $\propto (900\ \mathrm{kgm}^{-3}/\rho)^{1/3}$. The size of the simulation system is $4\lambda_{\rm cr} \times 4\lambda_{\rm cr}$, thus scaling with the size of the wakes ($\lambda_{\rm cr}/R \approx 150\tau {r_h}^3$); the side view covers $4\lambda_{\rm cr} \times 1\lambda_{\rm cr}$. The number of simulation particles $N \approx 116 \cdot 10^3 \tau^3 {r_h}^6$. The insert sketches the regimes where various physical factors dominate, based on the estimates given in the text. The dashed curves indicate $Q = 2$ in terms of $c_{rad}/(R\Omega)$: at the boundary between wakes and impacts $Q = 2$ corresponds to $c_{rad}/(R\Omega) = 3$.

this factor alone would be able to maintain.[36),42),51)] For a constant $\varepsilon_{\rm n} \lesssim 0.5$ (or the frosty particle model of Fig. 2) the minimum velocity dispersion due to impacts is $c_{imp}/(R\Omega) \sim 3$. Similarly, the gravitational encounters maintain a minimum velocity dispersion $c_{enc} \sim v_{esc}$, where $v_{esc} = \sqrt{2GM/R}$ is the escape speed. This can be expressed as $c_{enc}/(R\Omega) \approx 5{r_h}^{3/2}$. The gravitational encounters thus dominate over physical impacts for $r_h \gtrsim 0.7$. A rough criterion for the collective wake-structure is obtained by assuming that they appear whenever the minimum velocity dispersion drops below $Q \sim 2$. This corresponds to $c_{wake}/(R\Omega) \sim 10Q\tau {r_h}^3 \sim 20\tau {r_h}^3$. Thus $c_{wake} > c_{imp}$ (or $c_{wake} > c_{enc}$) defines the sketched boundary between wakes and impacts (or encounters). The other dashed curves in the insert indicate where $Q = 2$ corresponds to $c_{rad}/(R\Omega) = 5, 10, 20$.

The effect of gravity wakes on viscosity is depicted in Fig. 6. For $\tau \gtrsim 0.5$ and

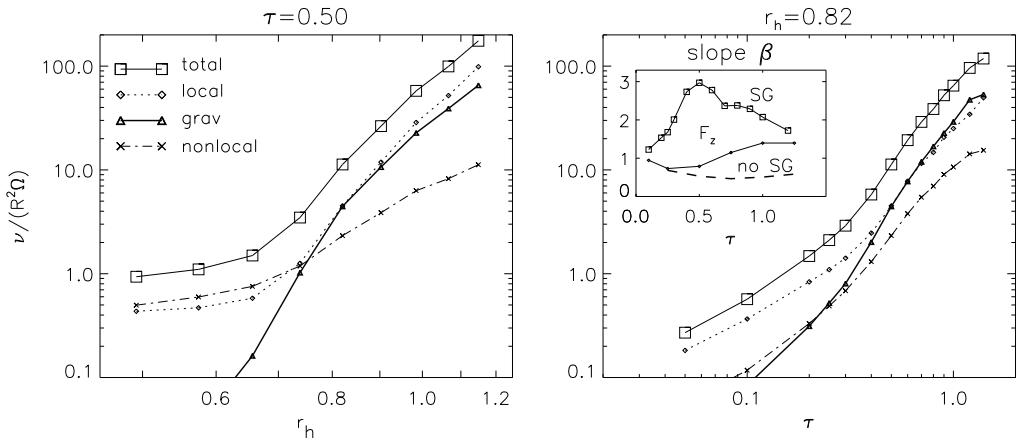

Fig. 6. Comparison of various contributions to total viscosity, in a) as a function of r_h for $\tau = 0.5$ and b) as a function of τ for r_h. They correspond to the $\varepsilon_{\rm n} = 0.5$ simulations depicted in Fig. 5. The insert in b) displays the slope of $\nu \propto \tau^{\beta}$, reaching values $\beta \approx 2$ for $\tau \sim 1$; for comparison nongravitating simulations (dashed curve) and simulations with just vertical self-gravity (solid curve are also depicted.

$r_h \gtrsim 0.75$, the ν_{grav} contribution associated with the gravitational torques from inclined wakes become dominant.[13),57)] Also ν_l is strongly enhanced due to systematic motions associated with the wakes, whereas the ν_{nl} is almost insignificant. Systematic motions also lead to local vertical thickening when individual wakes clash together, seen in the vertical profiles of Fig. 5. The results of Fig. 6 agree with the trends originally found,[13)]

$$\nu_{tot} \approx (\nu_{grav} + \nu_l) \approx 2\nu_{grav} \propto {r_h}^5 G^2 \Sigma^2 / \Omega^3. \qquad (3{\cdot}5)$$

The Σ^2 ($\propto \tau^2$ in the figure) dependence is similar to the standard continuum fluid formula for spiral torques in galaxy disks,[30)] while the r_h dependence can be interpreted as an effect related to finite size of particles: the smaller the r_h, the closer is the scale of wakes compared to physical size of particles. This limits the maximum contrast the wakes can attain (spatial density of wakes is limited by the internal density of particles).

In the above wake survey (Fig. 5), $\varepsilon_{\rm n} = 0.5$ was adopted. In the case of more dissipative impacts (or with the 'frosty' particle model of Fig. 2), the overall picture would be more or less the same. However, for less dissipative impacts the wake structure can be significantly weaker for a given τ and r_h. For example, using the same parameter values as in Fig. 3c), there is hardly any trace of wakes in a corresponding simulation using the smooth particle model of Fig. 2. This is to be expected, since according to Fig. 2b), the impacts alone will now maintain $c_{rad}/(R\Omega) \sim 20$ at $\tau = 0.75$; this corresponds to $Q \approx 5$, thus suppressing any wakes. On the hand, the same smooth particle elasticity model leads to clear wake structure for $\tau \gtrsim 1$. (Fig. 7).

The wake structure is also affected by the particle size distribution (Fig. 8). Although the large particles still form distinct wakes, the overall contrast is reduced due to the more uniform distribution of small particles. This implies that a system can exhibit dynamically significant wake structure, though it might be more hidden in photometric observations.[45)]

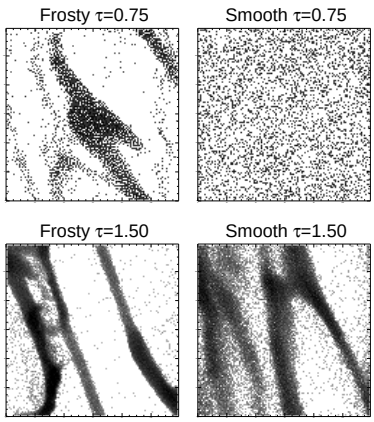

Fig. 7. Comparison of simulations with frosty and smooth particle elasticity models for $\tau = 0.75$ and $\tau = 1.5$. Snapshots are from $2\lambda_{\rm cr} \times 2\lambda_{\rm cr}$ simulations with $r_h = 0.82$.

Several types of observations have confirmed the existence of self-gravity wakes in Saturn's rings: although unresolved (wake scale $\sim$ 100 meters), they lead to a global signature on how the rings reflect and transmit light. For example, the long-known *azimuthal brightness asymmetry*[*)] is quantitatively explained[17),38),45)] by the trailing wakes, systematically tilted by $\sim 20^\circ$ with respect to azimuthal direction. Wakes are detected in the radar-echo of rings,[34)] as well as on how the Saturn microwave radiation is transmitted through the rings.[15)] The estimates of ring viscosity based on the damping of A ring density satellite density waves[59)] also agree with the ν_{grav} formula of Ref. 13). Currently the wakes are probed in detail via the various Cassini stellar occultation observations,[8),9),19),58)] providing important constraints for the physical properties and size distribution of unseen individual ring particles.

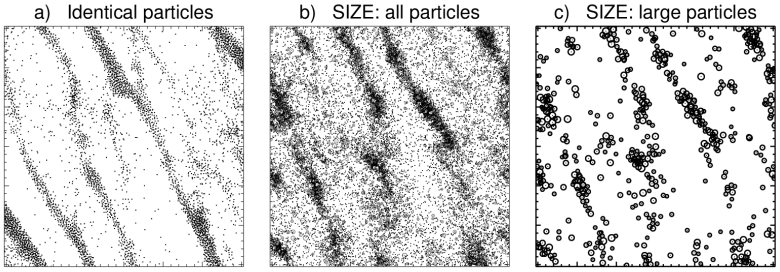

Fig. 8. a) Identical particle simulation with $\tau = 0.5$, $r_h = 0.85$, using 'frosty' particle elasticity model. b) Simulation with same parameters, except having $q = -3$ power-law size distribution with $R_{max}/R_{min} = 10$. c) Particles with $R > R_{max}/2$ shown separately.

[*)] The ring brightness in a given distance depends on ring longitude ϕ in a bi-symmetric manner:[14),17)] for example in the ground-based observations the brightness exhibits minima at $\phi \sim 70^\circ$ and $\sim 250^\circ$ with respect to sub-observer direction. The largest variation, $\pm$20%, occurs in the mid-A ring when the rings are viewed at $\sim 15^\circ$ opening angle; the minimum corresponds to ring longitudes where the wakes are viewed along their average long-axis.

§4. Viscous instability and overstability

The Voyager and Cassini data have revealed overwhelming amount of fine structure in Saturn's rings. Much of this is connected to perturbations by external satellites (in particular in the outer A ring), but many mysteries remain, for example what is the cause of the B ring optical depth jumps, where the optical depth suddenly drops from $\tau \sim 5$ to $\tau \sim 2$ in ~ 50 km wide regions.[10] Similarly, the overall structure of the C ring consists of moderately dense plateaus ($\tau \sim 0.5$) separated by hundreds of kilometers wide low optical depth ($\tau \sim 0.05$) regions.

Very early on, viscous instability was evoked[27),29),66] to explain such bimodal variations. In these models, the collisional flux of particles (proportional to dynamic viscosity $\eta = \nu\tau \propto \tau^{\beta+1}$) is directed toward density maxima (equivalent to $\beta < -1$), eventually establishing a state where the flux from dense but dynamically cool ringlets is balanced by the flux from rarefied, dynamically hot regions. Nevertheless, this model was soon discarded, mainly as the first laboratory measurements[5] indicated too dissipative particles for the instability mechanism to work.[2),67] Also, the observed structure did not agree with the predictions of the simple instability models, according to which the ring should separate into high τ ringlets surrounded by almost empty gaps.[21] Thus other alternatives gained attention, among them those related to the possibility that dense rings are viscously overstable.[4] In the axisymmetric overstability the radial particle flux is directed away from density maxima, like in a stable ring. However, the flux increases so strongly with density (large β), that the system overshoots in trying to smooth the density variations, instead leading to density oscillations. Although it appears unlikely that overstability could account for large scale structures in the densest rings,[26] there are clear indications of small-scale ~ 100 meter axisymmetric oscillations in moderate τ locations in the rings[9),58] likely to represent such overstable oscillations.

4.1. *Viscous overstability (oscillatory instability)*

The isothermal hydrodynamical models predicted that practically any flattened ring system (with $\beta \gtrsim 0$) should be overstable,[52] leading to growing axisymmetric oscillations in density and velocity components, eventually saturating at some finite amplitude via nonlinearity.[53] The mechanism itself was confirmed in direct N-body simulations, which however indicated a considerably more stringent condition for the onset of overstability, $\beta \gtrsim 1$.[44] This holds for nongravitating simulations (e.g. the smooth particle model is overstable for $\tau \gtrsim 4$ as anticipated from Fig. 2d), as well for simulations where the vertical self-gravity is approximated with an enhanced vertical central force (the trick $\Omega_z/\Omega > 1$, originally devised in Ref. 67), leading to $\beta > 1$ already for $\tau \sim 1$, in a similar fashion as in the case of actual vertical self-gravity (see the insert in Fig. 5).*) Transport coefficients derived from simulations with different values of Ω_z/Ω, in combination with improved non-isothermal hydrodynamical mod-

*) Same condition, $\beta \gtrsim 1$ works also in nongravitating 2D simulations, where the steep rise of ν_{nl} when the close-packing limit is approached, makes the system strongly overstable already for $\tau \gtrsim 0.4$. This fact was utilized in Ref. 43) to directly demonstrate overstability before it was technically feasible in 3D simulations.

els[44),49)] were useful in analyzing the linear growth of oscillations, and also allowed analytical treatment of saturation in weakly nonlinear case.[50)] Recently, significant progress has also been made using kinetic theory approach.[25)]

However, it is currently unclear what is the overstability condition for a fully self-gravitating ring. The simulations[44)] indicate that self-gravitating systems exhibit overstability for $\tau \gtrsim 1$, but only if the wake-structure is not too strong: see the upper left corner of Fig. 5 ($r_h \sim 0.6$). On the other hand, for stronger wakes the overstability is clearly suppressed, though the overstability condition $\beta \gtrsim 1$ should be satisfied by an ample margin (strong wakes imply $\beta \gtrsim 2$). This suppression might be related to different geometry and phase of the velocity and density oscillations for overstability and wakes, combined with the fact that they prefer practically similar wavelength range. In any case, even an approximative analytical theory is missing, making numerical simulations indispensable in looking the interplay of wakes/overstability.*)

Figure 9 illustrates the overstable oscillations (superposed with weak inclined wakes) in a dense system with moderate self-gravity ($\tau = 5, r_h = 0.65$). In contrast to systems with strong wakes at larger r_h, the τ now stays very high even at the density minima, thus reminiscent of the conditions at the B ring. If this type of behavior is typical to the densest part of the B ring ($r \sim$ 110 000 km), then according to the survey in Fig. 5 the internal density of particles should be about 300–450 kgm^{-3}, suggesting quite under-dense porous ice particles.

Unfortunately, the densest regions in the B ring are opaque (or very nearly), making it hard for stellar occultation experiments to obtain reliable optical depths. One possibility to check observationally for the presence of overstable oscillations is the shadows the density crests would cast when the solar elevation is small. Although the shadows would be non-resolved, they would make the ring brightness depend on the azimuth (predicted amplitude $\sim 10\%$ at 5° solar illumination angle).[48)] How-

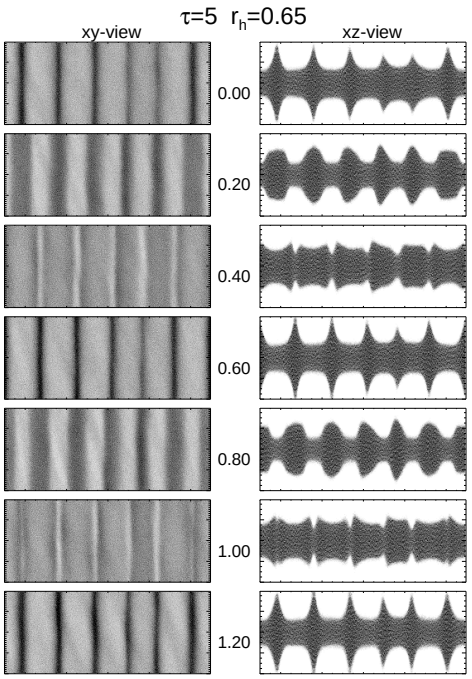

Fig. 9. Overstable oscillations followed over one oscillation period ($\sim$ 1.2 orbital periods; the prolongation is due to self-gravity). The calculation region is 1000 $\times$ 400 particle radii. Note the vertical 'splashing',[4)] the ring behaving in a nearly incompressible manner: the vertical scale in the plot is exaggerated by factor 10.

*) Unfortunately the technical requirements are quite demanding: ideally, the size of simulations should be several tens of $\lambda_{\rm cr}$'s (Fig. 9 corresponds to just $5\lambda_{\rm cr} \times 2\lambda_{\rm cr}$, even with $N = 270\,000$ particles.

ever, observing such a signature, even if present, is complicated.

4.2. *Viscous instability*

In the case of viscous instability, the hydrodynamic stability criterion $\beta < -1$ is fully consistent with direct N-body simulations, although the minimum unstable wavelengths (~ 200 particle radii) are about a magnitude longer than what simple hydrodynamical linear stability analysis predicts.[46] Figure 10 displays larger-scale simulation with the frosty particle elasticity model, which leads to spontaneous amplification of density fluctuations for $0.75 \lesssim \tau \lesssim 2$.

Figure 11 depicts in more detail the structure resulting from viscous instability, characterized by a (near) balance of radial particle flux between flattened dense ringlets surrounded by rarefied, large velocity dispersion regions. In particular, Fig. 11c) shows the profile of dynamic viscosity, which in this nonlinear quasi steady-state has practically constant value (though one of the ringlets corresponds to local bump in η and is accordingly slowly dissolving). With time, the ringlets slowly merge, the typical separation growing $\propto \sqrt{t}$. Thus at least in principle, large scale structure may emerge as a result of viscous instability.[46]

Nowadays, viscous instability is typically disregarded as a candidate for the ring fine-structure, basically since it requires fairly elastic particles in order to operate. In such a case the self-gravity wakes are harder to form. Thus the observed wake structure in the A and B ring is usually taken as an evidence against elastic particles

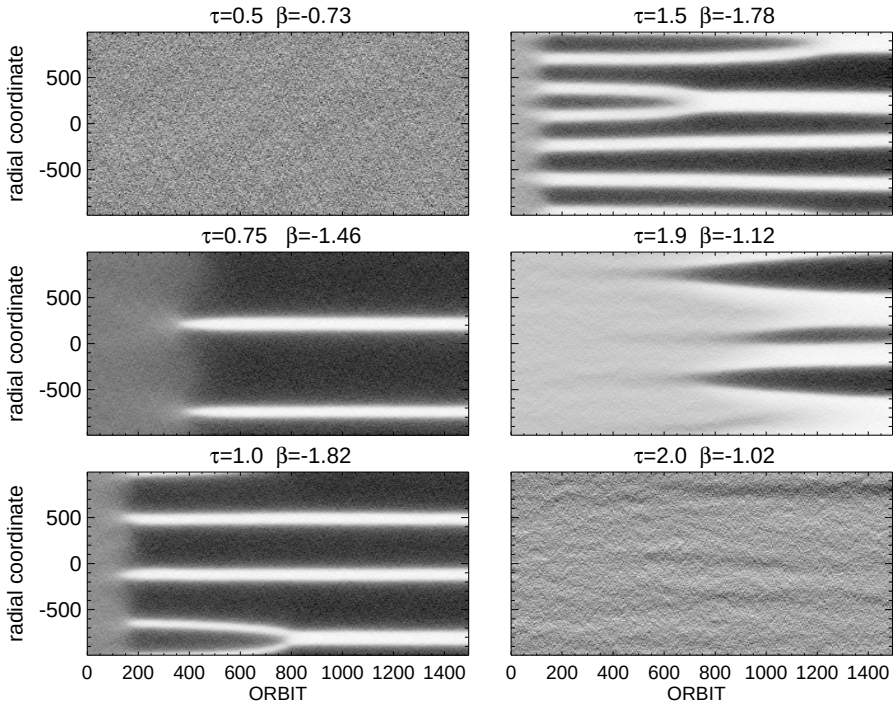

Fig. 10. Emergence of viscous instability in larger-scale simulations[46] using the frosty particle elasticity model. The value of β is for the uniform initial state, $\beta \leq -1$ indicates linear instability.

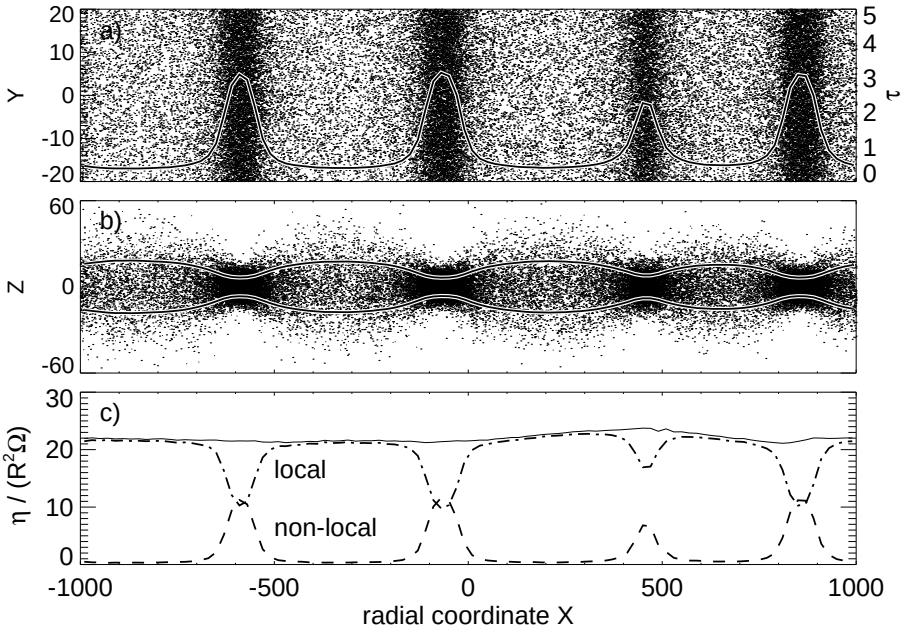

Fig. 11. Nonlinear radial balance between dense and rarefied regions resulting from viscous instability. The upper two frames show the top a) and side views b) of the simulation with $\tau = 0.92$, using the smooth particle elasticity model. The frame c) depicts the dynamic viscosity profile (solid curve), showing also separately the local and nonlocal contributions.[46)]

— though based on Fig. 7, this argument is perhaps not as solid as typically assumed. It is also important to keep in mind that even the 'standard' frosty particle model would imply instability, if the effective particle size were smaller than the nominal 1 meter assumed in Fig. 2 ($R \lesssim 5$ cm would make it unstable; what matters is the low τ velocity dispersion in terms of $c/(R\Omega)$).[46)] Nevertheless, the basic instability model always requires a balance between a rarefied and a dense region, and thus, although it might have relevance in the C ring, does clearly not apply to the structure of the dense B ring.

There is an interesting variant of the standard instability model, the possibility of selective instability of small particles against the more uniform background of larger ones. Direct simulations[46)] indicate that such a situation is possible if the coefficient of restitution is smaller in impacts between small particles, than in impacts involving large particles. Such size-dependence of $\varepsilon_{\rm n}$ adds a new degree of freedom to the system, and in principle allows a balance of radial flux also between two dense regions. Importantly, the contrast can also have very different values depending on the details of the elasticity model assumed (Fig. 12). Nevertheless, this mechanism has yet been very little studied, and due to lack of relevant measurements it remains unclear whether real particles possess suitable size dependence of $\varepsilon_{\rm n}$ leading to this type of instability.

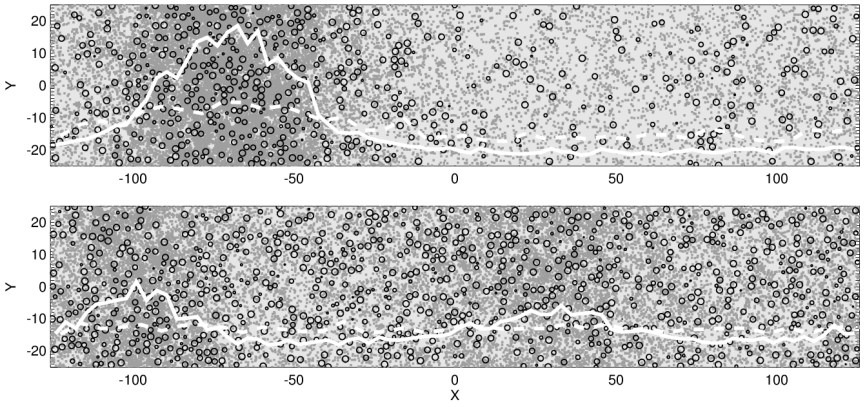

Fig. 12. Two examples of *selective viscous instability* in simulations (viewed from above, after 700 orbital periods). The systems consist of two particle sizes with R_2/R_1=3, and $\tau_1 = \tau_2 = 0.5$. Small (large) particles are indicated by gray (black) color, and the solid (dashed) white curve indicates their radial density profile. In the upper frame the impacts between small particles are much more inelastic than those between large particles, leading to strong density contrast among the small particles. In the lower frame the size-dependence of elasticity is smaller, leading to less pronounced variations. For exact parameter values, see Figs. 21 and 22 in Ref. 46).

§5. Summary

Saturn's rings provide an ideal laboratory to study the dynamics of astrophysical disks.[7] Dissipative impacts keep the system cold (the ratio of random velocities to rotation speed is $\sim 10^{-6}$ times that in galaxies), making it sensitive to viscous and gravitational disturbances. The time scales of local and global evolution are widely separated, allowing to study the local steady-state and the emergence of radial fine-structure separately from the origin of the whole ring system. There is also plenty of external and internal stirring in the rings: the response to perturbations gives important clues for particle properties.

The existence of self-gravity wakes in Saturn's rings, first predicted in computer simulations[41] (see also Ref. 62) has since then been confirmed by many types of observations. Their presence seems to favor fairly dissipative, under-dense particles — though it is good to remember that the parameter ranges of existing simulation surveys are far from exhaustive. The viscous overstabilities and instabilities are also obtained readily in simulations, though it is less clear if and how they connect to the actual ring structure. Nevertheless, it seems that almost any type of fine-structure generated in the computer sooner or later finds some counterpart in observations: the problem is that there is much more structure in the rings (in particular in the B ring) than can be explained by existing models.

There are important mechanisms not addressed in this brief review, like the adhesive forces between ring particles,[1] and the possibility that the ring particles have significant regolith on their surfaces (which can be released on perturbed regions, see e.g. the supplement of Ref. 55). The ring 'particles' themselves could

in fact be rubble-piles of small basic unit particles, with the measured size distribution manifesting the balance of accretion and fragmentation.[3),37)] The realistic simulation of such processes would require significantly larger N than so far used, preferentially of the order of 10^7 particles or more. Same holds for direct simulation of other outstanding problems, like the migration of propellers, the dynamics of perturbed ring edges, or the damping of satellite density waves. Hopefully there will be a breakthrough in the near future, either by the use of special processors, like the GRAPE (see the poster by Fujii et al. in these proceedings) or by the development of simulation codes suitable for large-scale parallel computing.

Finally, the power of combining dynamical and photometric modeling[38),45)] must be stressed. Detailed models of the azimuthal asymmetry and wakes[17)] are one example; other recent one is the successful reconciliation of observed ring opposition brightening with dynamical models with a realistic particle size distribution.[47)]

Acknowledgements

This work was supported by the Academy of Finland.

Appendix A
—— Local Simulation Method ——

A.1. *Dynamical equations*

In the local simulation method the calculations are restricted to a small comoving region, using linearized equations, $\ddot{x} - 2\Omega\dot{y} + ({\Omega_r}^2 - 4\Omega^2)x = F_x$, $\ddot{y} + 2\Omega\dot{x} = F_y$, $\ddot{z} + {\Omega_z}^2 z = F_z$, where x denotes radial direction, y the direction of orbital motion, and z is perpendicular to the equatorial plane. The coordinate system moves with angular velocity Ω in a circular orbit at a radial distance r. For a central point mass, the epicyclic (radial) frequency Ω_r and the vertical frequency Ω_z equal Ω. The $\vec{F}$ denotes additional forces, e.g. due to impacts or self-gravity. When $\vec{F} = 0$ these equations describe epicycles: the guiding centers drift with the velocity $({\Omega_r}^2 - 4\Omega^2)/(2\Omega)x$, which reduces to $-\frac{3}{2}\Omega x$ for a central point mass.

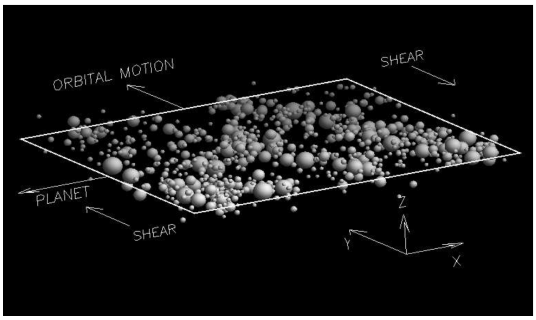

Fig. 13. Coordinate system of local simulations.

A.2. *Boundary conditions*

The particles leaving the simulation system (Fig. 13) are treated with periodic boundary conditions ('sliding-brick method').[62),67)] If the crossing occurs across the inner or outer radial boundary, the velocity is modified by $\Delta\dot{y} = \pm 3/2\ \Omega L_x$, which corresponds to the difference of shear velocity across the radial size L_x of the calculation cell. It is important to note that there is nothing special about the boundaries: exactly same shear is present

in every point of the system. The results are independent of the origin of the coordinate system, and the size of the calculation region, provided that it is large compared to the mean free path between impacts.*)

A.3. *Treatment of impacts*

Two different treatments are used for collisions: these are either modeled as instantaneous velocity changes[39),41),64)] or by including impact forces between any (slightly) overlapping particle pair.[32),42)] In the former case, the impact outcome is determined by the coefficient of normal ($0 \leq \varepsilon_{\rm n} \leq 1$) and tangential restitution ($-1 \leq \epsilon_t \leq 1$). If $\epsilon_t \neq 1$, the particle spins need also to be included. A simple model for slightly non-spherical shape has also been studied, by assuming that the tangent plane of impact is randomly tilted (by a small amount) with respect to the line joining the colliding particles.[40)] From the change of relative velocity, the individual changes are determined by the conservation of linear and angular momentum.

With gravitating particles, in particular in the regime where gravity leads to the formation of semi-permanent aggregates[24),42)] the instantaneous impact method easily fails: the net attraction between a particle pair can be directed toward each other, even in the case when their post-collisional velocity difference is zero, which will lead to overlap on the next step. Instead of artificially pushing the particles apart, one can include an supporting pressure force during the impact. A convenient choice is a simple visco-elastic force $F(\alpha) = k_1\alpha + k_2\dot{\alpha}$, between any slightly penetrating particle pair ($\alpha > 0$ denotes the penetration depth). The CPU-time consumption is tolerable, provided that the impact duration T_{dur} is chosen not too short compared to dynamical timescales of interest.**)

A.4. *Search of impact pairs*

The speed of simulations depends critically on the efficient search of impact pairs. In their seminal non-gravitating local simulations Ref. 67) used the fact that orbits between impacts are Keplerian epicycles, and solved iteratively for the intersection time of each pair of epicycles. The pair with the smallest impact time was chosen and their post-impact orbital elements were calculated, leading to updated intersection times with all the other particles. The system was thus moved from one impact to the next ("event-driven" method). For larger N it is advantageous to integrate the equations of motions (this also allows inclusion of additional forces), and during each time-step search for potential interactions among the neighboring particles. Among this list, the impacts are executed and the list updated as in the event-

*) Note that periodic boundaries assume that the ring is homogeneous in planar directions: different treatment is needed for example when simulating propeller structures around an embedded moonlet, where the symmetry between incoming unperturbed flow and the perturbed outgoing flow is broken (see e.g. Refs. 28), 31), and 54)). Similarly, modified boundary treatment has been used in the case of modeling the local response to a passing satellite density wave;[33)] fully general simulation of density waves probably requires the use of azimuthally complete simulation.[22)]

**) The attractive feature of the linear model is that the constants k_1 and k_2 are easily tied to the desired T_{dur} and $\varepsilon_{\rm n}$. Friction has also been included.[32),42)] The results are identical to those with instantaneous impacts, as long as $T_{dur} \lesssim 10^{-3}$ orbital periods.[42)] In future more realistic impact[6)] and adhesion[65)] models could also be used.

driven method. The number of neighbors examined for potential impacts can be controlled by keeping track of the maximum pre-step separation which has led to an impact during previous steps. In the optimal case the number of pairs examined is proportional to $cN/(R\Omega)$.

A.5. *Treatment of self-gravity*

Inclusion of self-gravity increases the computational burden significantly: besides the calculation of forces themselves, the enhanced impact frequency and velocity dispersion slow down the collisional calculations. Also, larger N is needed as the size of the calculation cell must be large compared to the size of the wake structures. In the optimal case, about equal time is spent in the calculation of gravity and impacts: to achieve this, it is important not to use too short time step in the gravitational calculations (it is usually sufficient to do force evaluations at most ~ 500 times/orbital period, while the impact calculations might use an order of magnitude shorter steps).

The calculation of gravitational forces has been done either with direct summation, or in the case of large N, with a combination of direct summation for the nearby particle pairs (say within $\Delta < \Delta_{\rm min} \sim 0.25\lambda_{\rm cr}$) and a 3-dimensional grid evaluation for the distant gravity (inside $\Delta_{\rm min} < \Delta < \Delta_{\rm max} = \min(L_x, L_y)$) with FFT utilizing the periodicity in planar (sheared) coordinates.[44] A tree-method is also used,[39] but there is no clear advantage over the use of grid (at very large N it might even be slower): the nearby forces must in every case be evaluated accurately, in order to include correctly the heating by binary encounters. A correction for the overall vertical self-gravity from $\Delta > \Delta_{\rm max}$ is easy to include analytically. A fast approximative treatment of strictly axisymmetric gravity is also possible, using a superposition of analytically evaluated forces from a plane-wave decomposition.[46]

A.6. *Tabulation*

An essential part of any simulation code, besides storing snapshots of the system, is to tabulate time-averages of various quantities of interest, (impact frequency, components of pressure tensor, radial and vertical profiles, Fourier coefficients etc.). For most part this can be done in conjunction with impact and gravity calculations.

References

1) N. Albers and F. Spahn, Icarus **181** (2006), 292.
2) S. Araki and S. Tremaine, Icarus **65** (1986), 83.
3) A. Bodrova, J. Schmidt, F. Spahn and N. Brilliantov, Icarus, in press.
4) N. Borderies, P. Goldreich and S. Tremaine, Icarus **63** (1985), 406.
5) F. Bridges, A. Hatzes and D. Lin, Nature **309** (1984), 333.
6) N. V. Brilliantov, F. Spahn et al., Phys. Rev. E **53** (1996), 5382.
7) J. A. Burns and J. N Cuzzi, Science **312** (2006), 1753.
8) J. E. Colwell, L. W. Esposito and M. Sremcević, Geophys. Res. Lett. **33** (2006), L07201.
9) J. E. Colwell et al., Icarus **190** (2007), 127.
10) J. E. Colwell et al., in *Saturn from Cassini-Huygens*, ed. M. K. Dougherty, L. W. Esposito and T. Krimigis (Springer, 2009), p. 375.
11) J. N. Cuzzi, J. A. Burns, R. H. Durisen and P. M. Hamill, Nature **281** (1979), 202.
12) J. N. Cuzzi, J. A. Burns et al., Science **327** (2010), 1470.
13) H. Daisaka, H. Tanaka and S. Ida, Icarus **154** (2001), 296.
14) L. Dones, J. N. Cuzzi and R. M. Showalter, Icarus **105** (1993), 184.
15) D. Dunn et al., Icarus **171** (2004), 183.

16) P. Goldreich and S. Tremaine, Icarus **34** (1978), 227.
17) R. G. French, H. Salo, C. A. McGhee and L. Dones, Icarus **189** (2007), 493.
18) A. P. Hatzes, F. G. Bridges and D. N. C. Lin, Mon. Not. R. Astron. Soc. **231** (1988), 1091.
19) M. M. Hedman et al., Astron. J. **133** (2007), 2624.
20) M. M. Hedman et al., Science **332** (2011), 708.
21) K. A. Hämeen-Anttila, Astrophys. Space Sci. **58** (1978), 477.
22) J. Hänninen and H. Salo, Icarus **97** (1992), 228.
23) W. H. Julian and A. Toomre, Astrophys. J. **146** (1966), 810.
24) R. Karjalainen and H. Salo, Icarus **172** (2004), 328.
25) H. N. Latter and G. I. Ogilvie, Icarus **195** (2008), 725.
26) H. N. Latter and G. I. Ogilvie, Icarus **210** (2010), 318.
27) D. N. C. Lin and P. Bodenheimer, Astrophys. J. **248** (1981), L83.
28) M. Lewis and G. R. Stewart, Icarus **199** (2009), 387.
29) J. Lukkari, Nature **292** (1981), 433.
30) D. Lynden-Bell and A. Kalnajs, Mon. Not. R. Astron. Soc. **157** (1972), 1.
31) S. Michikoshi and E. Kokubo, Astrophys. J. Lett. **732** (2011), L23.
32) R. Morishima and H. Salo, Icarus **181** (2006), 272.
33) I. Mosqueira, Icarus **122** (1996), 128.
34) P. D. Nicholson et al., Icarus **177** (2005), 32.
35) K. Ohtsuki, Icarus **106** (1993), 228.
36) K. Ohtsuki and H. Emori, Astron J. **119** (2000), 403.
37) R. P. Perrine, D. C. Richardson and D. J. Scheeres, Icarus **212** (2011), 719.
38) C. C. Porco et al., Astron J. **136** (2008), 2172.
39) D. C. Richardson, Mon. Not. R. Astron. Soc. **269** (1994), 493.
40) H. Salo, Icarus **70** (1987), 37.
41) H. Salo, Nature **359** (1992), 619.
42) H. Salo, Icarus **117** (1995), 287.
43) H. Salo, Lecture Notes in Phys. **564** (2001), 330.
44) H. Salo, J. Schmidt and F. Spahn, Icarus **153** (2001), 295.
45) H. Salo, R. Karjalainen and R. G. French, Icarus **170** (2004), 70.
46) H. Salo and J. Schmidt, Icarus **206** (2010), 390.
47) H. Salo and R. G. French, Icarus **210** (2010), 785.
48) H. Salo and J. Schmidt, Abstracts of EPSC-DPS Joint Meeting 2011.
49) J. Schmidt, H. Salo, F. Spahn and O. Petzschmann, Icarus **153** (2001), 316.
50) J. Schmidt and H. Salo, Phys. Rev. Lett. **90** (2003), 061102.
51) J. Schmidt, K. Ohtsuki, N. Rappaport, H. Salo and F. Spahn, in *Saturn from Cassini-Huygens*, ed. M. K. Dougherty, L. W. Esposito and T. Krimigis (Springer, 2009), p. 413.
52) U. Schmit and W. M. Tscharnuter, Icarus **115** (1995), 304.
53) U. Schmit and W. M. Tscharnuter, Icarus **138** (1999), 173
54) M. Seiss, F. Spahn, M. Sremcevíc and H. Salo, Geophys. Res. Lett. **32** (2005), L11205.
55) M. Sremcević, J. Schmidt, H. Salo, M. Seiss, F. Spahn and N. Albers, Nature **449** (2007), 1019.
56) G. R. Stewart, D. N. C. Lin and P. Bodenheimer, in *Planetary Rings*, ed. R. Greenberg and A. Brahic (Univ. of Arizona Press, Tucson, 1984), p. 447.
57) H. Tanaka, K. Ohtsuki and H. Daisaka, Icarus **161** (2003), 144.
58) F. S. Thomson, E. A. Marouf et al., Gepohys. Res. Lett. **34** (2007), L24293.1.
59) M. S. Tiscareno, J. A. Burns et al., Icarus **189** (2007), 14.
60) A. Toomre, Astrophys. J. **139** (1964), 1217.
61) A. Toomre, in *Structure and Evolution of Normal Galaxies*, ed. S. M. Fall and D. Lynden-Bell (1981), p. 111.
62) A. Toomre and A. J. Kalnajs, in *Dynamics of Disc Galaxies*, ed. B. Sundelius (Almquist-Wiksell, Göteborg, 1991), p. 342.
63) S. Tremaine, Astron. J. **125** (2003), 894.
64) J. Trulsen, Astrophys. Space Sci. **17** (1972), 241.
65) K. Wada, H. Tanaka et al., Astrophys. J. **661** (2007), 320.
66) W. Ward, Geophys. Res. Lett. **8** (1981), 641.
67) J. Wisdom and S. Tremaine, Astron. J. **95** (1988), 925.